Original Article

Regional assessment of aortic valve calcification using topographic maps in contrast-enhanced CT: *in-vivo* sex and severity-based differences in calcific presentation

Mohamed Abdelkhalek[1]^, MohammadAli Daeian[2], Zahra Keshavarz-Motamed[1,2,3]

[1]School of Biomedical Engineering, McMaster University, Hamilton, ON, Canada; [2]Department of Mechanical Engineering, McMaster University, Hamilton, ON, Canada; [3]School of Computational Science and Engineering, McMaster University, Hamilton, ON, Canada

Contributions: (I) Conception and design: M Abdelkhalek, Z Keshavarz-Motamed; (II) Administrative support: Z Keshavarz-Motamed; (III) Provision of study materials or patients: Z Keshavarz-Motamed; (IV) Collection and assembly of data: M Abdelkhalek; (V) Data analysis and interpretation: M Abdelkhalek, M Daeian; (VI) Manuscript writing: All authors; (VII) Final approval of manuscript: All authors.

Correspondence to: Prof. Zahra Keshavarz-Motamed, PhD. Department of Mechanical Engineering (Mail to JHE-310), McMaster University, Hamilton, Ontario, L8S 4L7, Canada; Department of Mechanical Engineering, McMaster University, Hamilton, ON, Canada; School of Computational Science and Engineering, McMaster University, Hamilton, ON, Canada. Email: motamedz@mcmaster.ca.

Background: Procedural planning for transcatheter aortic valve replacement (TAVR) is routinely performed using contrast computed tomography (CT) in patients with severe aortic stenosis (AS). Despite its potential, little investigation has been done into the possibility of aortic valve calcification (AVC) scoring in contrast-enhanced CT. Contrast CT has superior spatial and contrast resolution compared to the non-contrast Agatston score protocol, which would allow for development of better pattern and distribution descriptors of calcific lesions in the aortic valve (AV).

Methods: We developed a new false positive rate (FPR) based method that can quantify leaflet calcification based on shape overlap metrics. We also introduce a novel regional scheme for quantifying the shape and structure of calcification using topographic maps. The study was designed to: (I) determine the feasibility of using a novel method based on FPR to detect AVC using contrast-enhanced CT images by assessing the volume scores measured using FPR versus non-contrast methods and alternative contrast methods for volume scoring based on fixed or dynamic HU thresholds. (II) Develop a new scheme for assessing calcific geometry and structure and evaluate patterns of calcification in the varied presentation of AS.

Results: Our results show a very strong correlation with non-contrast volume ($r=0.919$, $P<0.001$; $n=178$) and Agatston scores ($r=0.913$, $P<0.001$; $n=178$) that were evaluated using a standard calcium scoring technique. Finally, we analyzed the differences and similarities in the patterns of calcific deposition with respect to sex and degree of severity.

Conclusions: The FPR method demonstrates the best overall agreement with non-contrast scores across both low and high ends of calcific density compared to luminal attenuation methods. In addition, we showed that leaflet calcific deposition follows distinctive patterns across the belly of the leaflet, with the rate of calcific progression peaking at the non-coronary cusp (NCC) leaflet and lowest for the right-coronary cusp. Females experience significantly lower calcific deposition compared to males despite showing similar patterns and symptoms. Our findings suggest that precise regional assessment of calcific progression could be an important tool for monitoring AS development as well as predicting peri-procedural complications in TAVR.

^ ORCID: 0000-0003-3981-9040.

Keywords: Aortic stenosis (AS); aortic valve calcium (AV calcium); computed tomography (CT); contrast-enhanced CT; transcatheter aortic valve replacement (TAVR); aortic valve replacement (AV replacement)

Submitted May 30, 2023. Accepted for publication Oct 10, 2023. Published online Nov 07, 2023.
doi: 10.21037/qims-23-778
View this article at: https://dx.doi.org/10.21037/qims-23-778

Introduction

Aortic valve calcification (AVC) strongly influences native and artificial valve behavior and is a key feature involved in the development and progression of aortic stenosis (AS) (1). AVC is presented in aortic sclerosis, a disease in which the valve leaflets begin to thicken and develop regions of focal calcification, and over time can progress to AS (1,2). AS is characterized as a gradual decrease of the valve orifice area leading to left ventricular outflow tract (LVOT) obstruction and left ventricular (LV) hypertrophy due to an increased afterload (3). Prior to the recent introduction of the minimally invasive transcatheter aortic valve replacement (TAVR), surgical aortic valve (AV) replacement was the only possible intervention for severe AS. As TAVR is becoming more frequent (4), the procedure is continuously advancing with improvements in valve and delivery system designs, as well as increased clinician experience (4). It is therefore critical that during procedural planning, valuable prognostic information is collected to help plan and optimize patient-specific interventions (5). Primarily, detailed calcification assessment must be included in this process (5,6) as AVC is associated with a variety of peri-procedural complications (5,7). In the context of TAVR, the new valve may be restricted from expanding completely due to native calcification. The presence of leaflet and/or LVOT calcification is a risk factor to paravalvular leakage surrounding the implant (8), annular rupture, aortic root (AR) injury or conduction abnormalities which may increase the risk of mortality (9,10).

Currently the only established method for assessing AVC quantitatively is via the Agatston method through non-contrast computed tomography (CT) images (11,12). Which was originally applied for quantifying coronary artery calcium (CAC) but has since been used to quantify cardiovascular calcification in various regions. In the case of the AV, it is measured at the cusp/leaflet region avoiding extra valvular calcium in the LVOT or the ascending aorta (11). Pixels above 130 Hounsfield unit (HU) are segmented and within each lesion in a 2D cross-section, the maximum HU is calculated and used to obtain a density weighting factor (DWF) which is multiplied by the 2D area of the lesion. The sum of this areas multiplied by DWF is then calculated to obtain the final Agatston score for the region of interest (11,12). It is primarily used as secondary diagnostic test for AS, when echocardiographic measures are discordant (6,11). However, this score has key limitations, it requires low resolution 2.5–3 mm axial views, which severely limits regional quantification of calcium burden (11,12). Furthermore, the lack of contrast precludes qualitative assessment of AV anatomy or valve planimetry (6). Both limitations motivate the design of new scoring method based on high resolution contrast CT images (13,14), especially in the context of TAVR, where accurate annular assessment using contrast CT is a necessity for procedural planning (6).

Previous studies (14-19) investigated simpler modifications to the standard Agatston technique when using contrast-enhanced CT images. These approaches were mainly motivated by the idea of using a new cut-off thresholding value, either fixed or dynamically determined based on luminal attenuation. In that regard, we previously (20) developed a method that does not explicitly rely on luminal attenuation. Instead, initial leaflet calcification regions are determined based on the intensity characteristics of a bounding AR segmentation. Using those initial conditions, an iterative region growing method adjusts the Hounsfield band for calcific detection gradually, until satisfying certain overlap criteria between calcific and non-calcific segments in the image. We were able to show strong correlation with gold standard non-contrast and echocardiographic based indices of AS severity (20). In this study we focused the study cohort on the tricuspid valve morphology and introduced a new anatomically based regional mapping scheme to provide a quantitative description of location, quantity, and average intensity of calcific deposition. The new topographic maps may provide a unique perspective for interpretation of calcific progression in terms of sex- and severity-based differences. To the best of our knowledge, this is the first study on *in-vivo* quantitative description of AV leaflet calcification using high resolution CT imaging.

Table 1 Baseline patient characteristics of study cohort

Category	Value
Age (years), mean ± SD	80.5±7.3
Sex, n (%)	
Female	80 (44.9)
Male	98 (55.1)
AS severity, n (%)	
Non severe	49 (27.5)
Severe	129 (72.5)
NYHA class, n (%)	
I	17 (9.6)
II	70 (39.3)
III	78 (43.8)
IV	13 (7.3)
Coronary artery disease, n (%)	85 (47.8)
Hypertension, n (%)	164 (92.1)
Type 2 diabetes mellitus, n (%)	74 (41.6)
Dyslipidemia, n (%)	132 (74.2)
Atrial fibrillation, n (%)	65 (36.5)

SD, standard deviation; NYHA, New York Heart Association; AS, aortic stenosis.

Methods

We evaluated the proposed method on a cohort of patients diagnosed with AS. We compared the scores using the proposed method on the contrast-enhanced images to the standard scores produced for non-contrast (16,18,21) images that were scored using commercially available software (Calcium scoring application, Syngo.via; Siemens Healtheneers, Forchheim, Germany).

Study population

We retrospectively selected 178 patients diagnosed with AS from Hamilton General Hospital (Hamilton, Canada; between 2020 and 2022). Non-consecutive data collection included patients evaluated for TAVR with severe or non-severe AS diagnosed by 2D doppler echocardiography and who underwent both gated contrast and non-contrast CT within 3 months of the echocardiogram. Severity was determined by recommended thresholds for AV area, peak aortic jet velocity and mean valve pressure gradient (22). The study was conducted in accordance with the Declaration of Helsinki (as revised in 2013). The study was approved by the Hamilton integrated research ethics board (HiREB) and individual consent for this retrospective analysis was waived. The selections were done by operators blinded to the objectives and contents of this study. Clinical measurements were performed per relevant guidelines and regulations including guidelines of the American College of Cardiology and American Heart Association. Demographic and procedural data were collected from the patients' medical records (see *Table 1* for patient characteristics).

CT acquisition

The patients underwent both contrast and non-contrast enhanced CT scans using GE Healthcare Discovery CT750 HD Scanner 64 slice 40 mm detector. Contrast CT images were acquired using retrospective gating without tube current modulation of the entire cardiac cycle using a slice thickness of 0.625 mm. Prospectively ECG gated non-contrast CT was performed in a sequential mode at 60–80% of the RR interval using a slice thickness of 3 mm (see Table S1 for CT acquisition parameters).

Computational analysis

Calcification detection

We developed a framework which consists of pipelines designed for the 3D visualization and quantification of calcific lesions using contrast-enhanced thoracic CT images (*Figures 1-6*; *Tables 1-4*). The proposed calcium detection method uses a novel segmentation scheme that is based on automatically detected local image features (*Figure 2*). The proposed method obviates the need for manual annotation of a region of interest in the ascending aorta or a predetermined minimum HU cutoff value. Our developed computational framework requires the field of view to be initially localized to the AV based on the standard assessment guidelines for TAVR planning (*Figure 1A*). A partial AR model is then automatically segmented (*Figure 1B*). Using the AR segmentation, principal directions and landmark points are generated semi-automatically (*Figure 1A,1B*). Using this initial set of parameters, a fully automatic detection scheme is designed to detect the maximal amount of calcific content regardless of the effect of the contrast agent on luminal attenuation (*Figure 2*). This is accomplished by measuring the false positive rate (FPR) between iterative decrements of HU threshold reconstructions of calcific segments and the partial AR model (*Figure 2*).

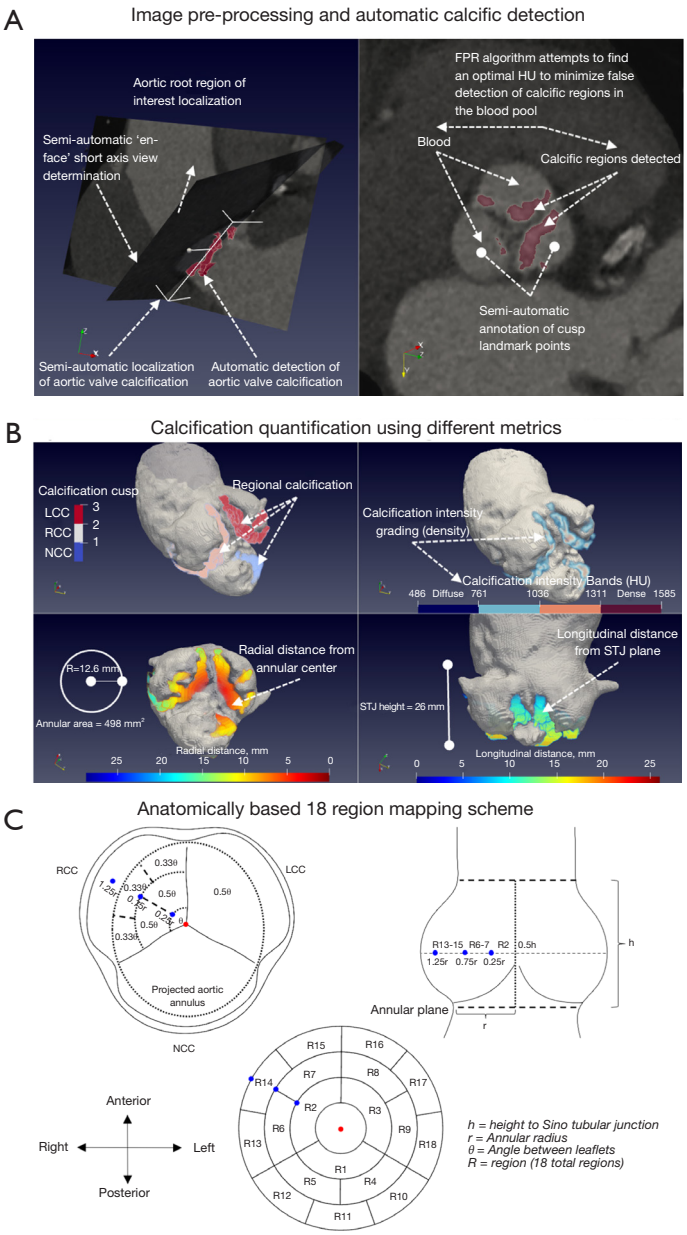

Figure 1 Framework for calcification assessment. Visual representation of the computational framework developed for the assessment of calcification pattern and structure in contrast enhanced CT images for AS. (A) Left: initial localization of AV; right: automatic calcific threshold determination based on automatic estimation of the ration between non-calcified lumen segments and calcific regions. (B) Different quantification color-coded maps from left to right; calcification separated by leaflet 1–3 corresponding to NCC, RCC and LCC respectively; radial distance map with range of [0-annular perimeter (mm)]; longitudinal distance map with range of [0-height of STJ (mm)]; HU intensity map for calcific lesions detected, color mapped by a fixed Hounsfield intensity range of 484–1,585 HU. The color bar is partitioned into 4 sections with 275.25 HU difference for each partition. (C) Schematic diagram of proposed anatomically based 18 region model of the aortic valve, regions are counted in clockwise order started from the NCC. Region subdivisions are based on parametric coordinates in cylindrical coordinate system, normalized by patient specific aortic root dimensional measurements (STJ height h, annular area derived radius r and angles θ between the interleaflet edges measured from the "en-face" short axis view of the valve. FPR, false positive rate; NCC, non-coronary cusp; RCC, right coronary cusp; LCC, left coronary cusp; HU, Hounsfield unit; STJ, sino-tubular junction; CT, computed tomography; AS, aortic stenosis; AV, aortic valve.

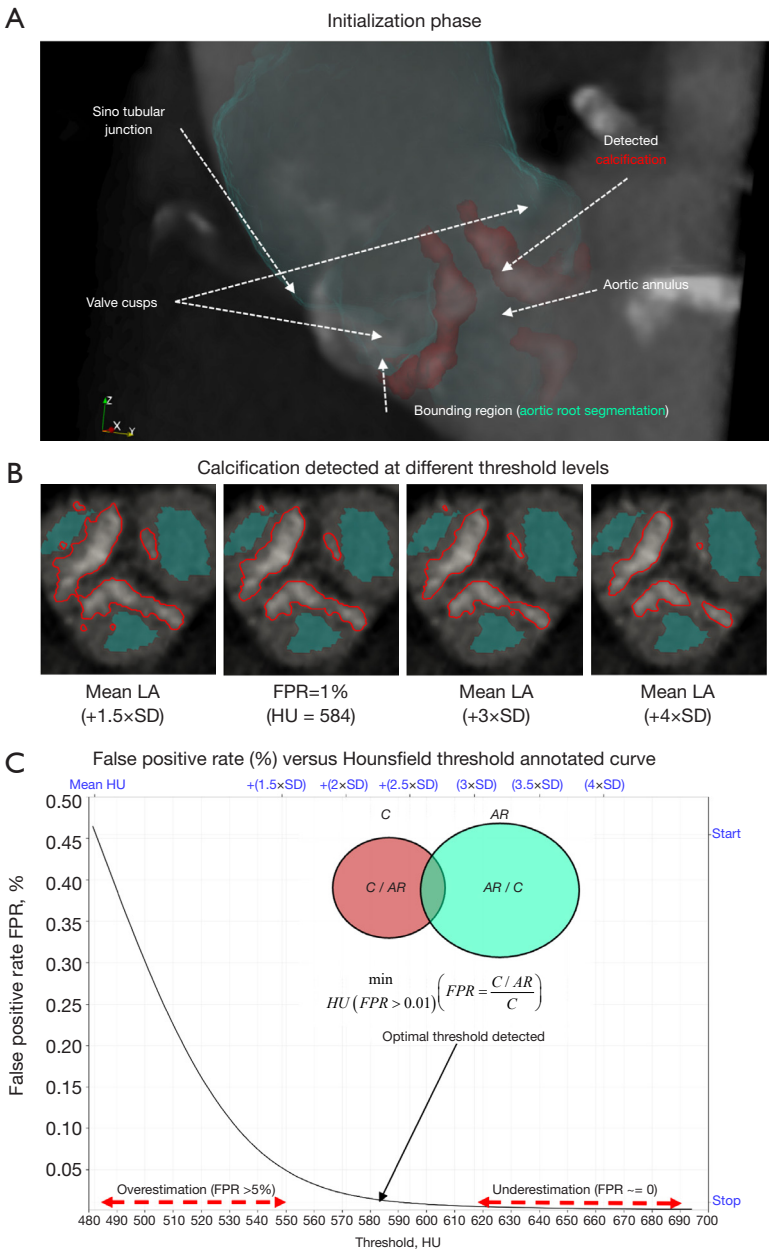

Figure 2 Calcification detection algorithm. Visual representation of the proposed algorithm for calcification detection in contrast enhanced CT. (A) Initialization step with automatically detected aortic root segmentation and "en-face" short axis view of leaflets. (B) 2D short-axis section of the aortic valve with overlaid contours of detected calcium segments in red and partial aortic root lumen in cyan using the different methods. (C) FPR *vs.* threshold curve measuring the rate of calcific pixels classified as non-calcific lumen segments, we exhaustively search for an optimal threshold in a wide HU band. Such that the resulting calcific segmentation is neither under nor over estimated. LA, luminal attenuation; SD, standard deviation; AR, aortic root; CT, computed tomography; FPR, false positive rate; HU, Hounsfield unit.

Assessment of the calcification detection method

Appropriate statistical tests were performed using Jamovi v.1.8. Summaries of the variables and tests performed in (*Figures 4,6*; *Tables 2-4*) are outlined as follows. Correlations and comparisons between the variables were performed using Spearman's rank correlation test, Wilcoxon rank paired *t*-test, non-parametric One-way ANOVA (Kruskal-Wallis) followed by post-hoc Dwass-Steel-Critchlow-

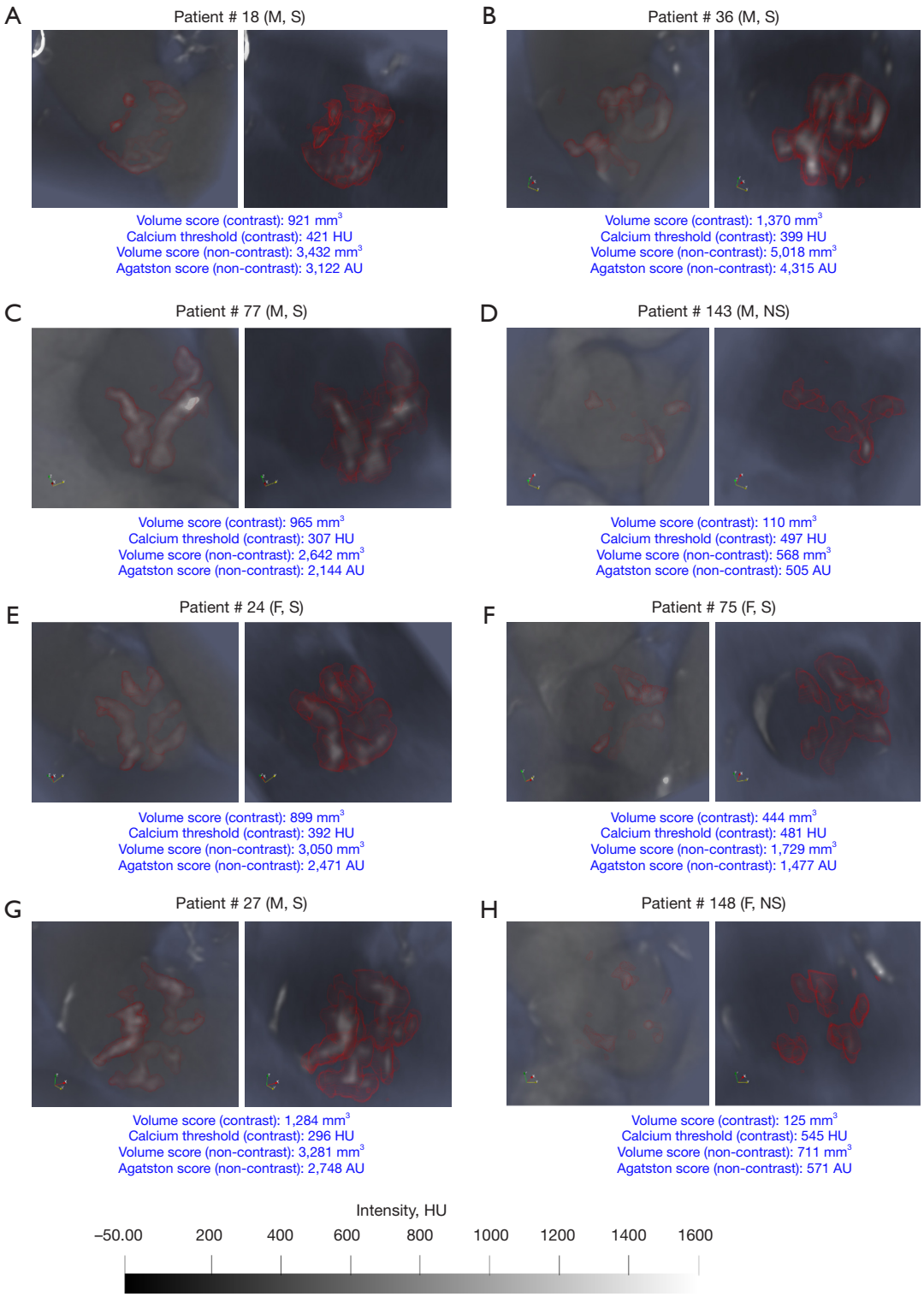

Figure 3 Amount of calcification in contrast vs. non-contrast (representative cases). (A-H) Eight patients were selected around the median volume score grouped by sex (M-F) and AS severity (NS-S). The left panel shows the detected calcification in the same patient using contrast enhanced images. The right panel shows the detected calcification in the same patient using non-contrast images. Field of view, orientation and opacity mapping matching was ensured to facilitate comparison. M, male; F, female; NS, non-severe; S, severe; AS, aortic stenosis; HU, Hounsfield unit.

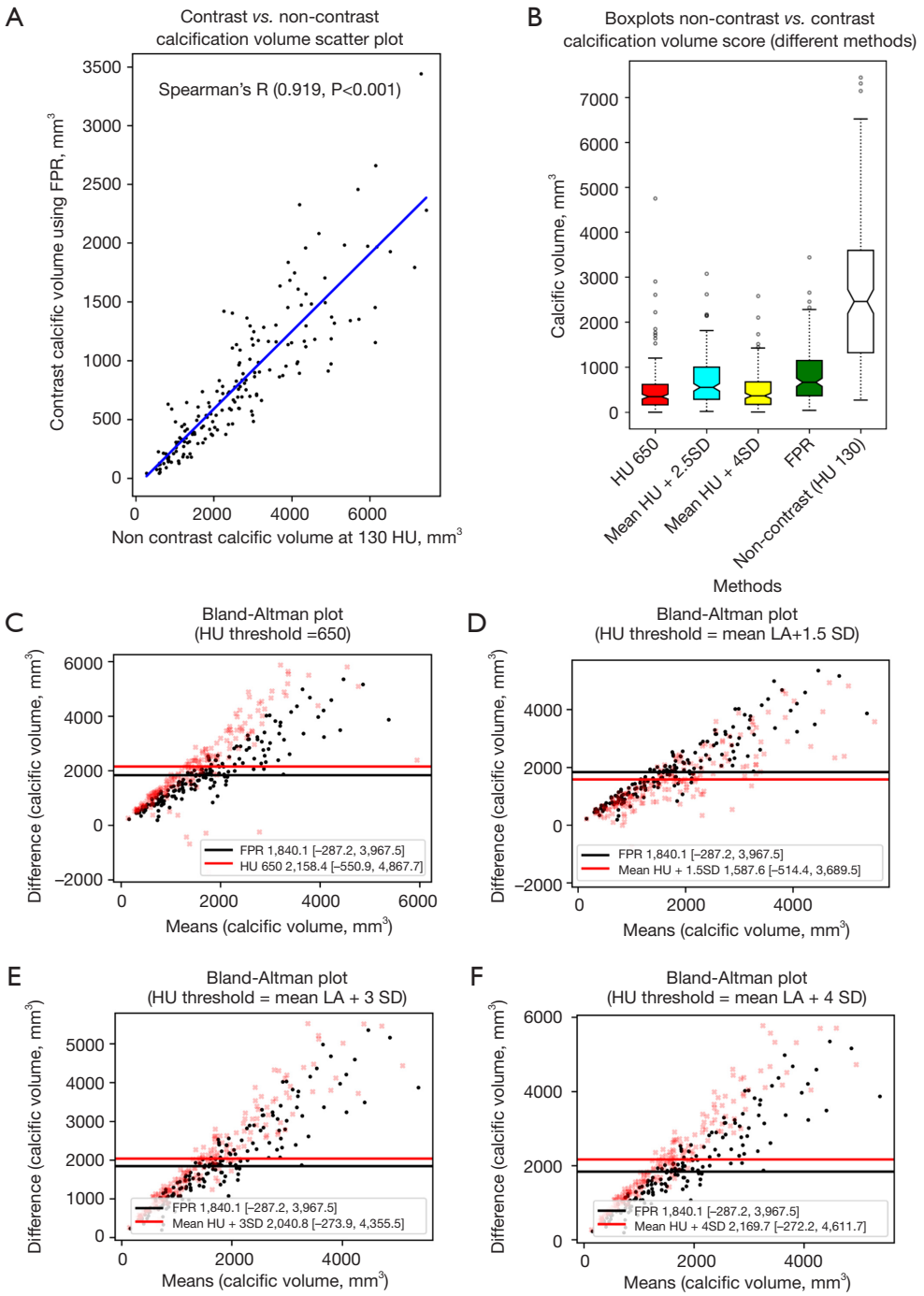

Figure 4 Statistics and data plots for parameters (N=178). (A) Scatter plot of contrast *vs.* non-contrast calcific volume; (B) boxplot comparing contrast (different methods *vs.* non-contrast calcific volume; (C-F) Bland-Altman plot of differences. HU, Hounsfield unit; SD, standard deviation; FPR, false positive rate; LA, luminal attenuation.

Fligner pairwise comparisons where applicable. Bland-Altman analysis of difference was used to compare the developed FPR method alongside the conventional methods based on a fixed HU threshold [650] or a mean HU attenuation at the ascending aorta (+1.5SD, +2.5SD, +3SD, +3.5SD, +4SD) (*Figures 4,6A*). Values were reported as median [25th–75th percentile], mean ± standard deviation or mean difference [lower limit of agreement, upper limit

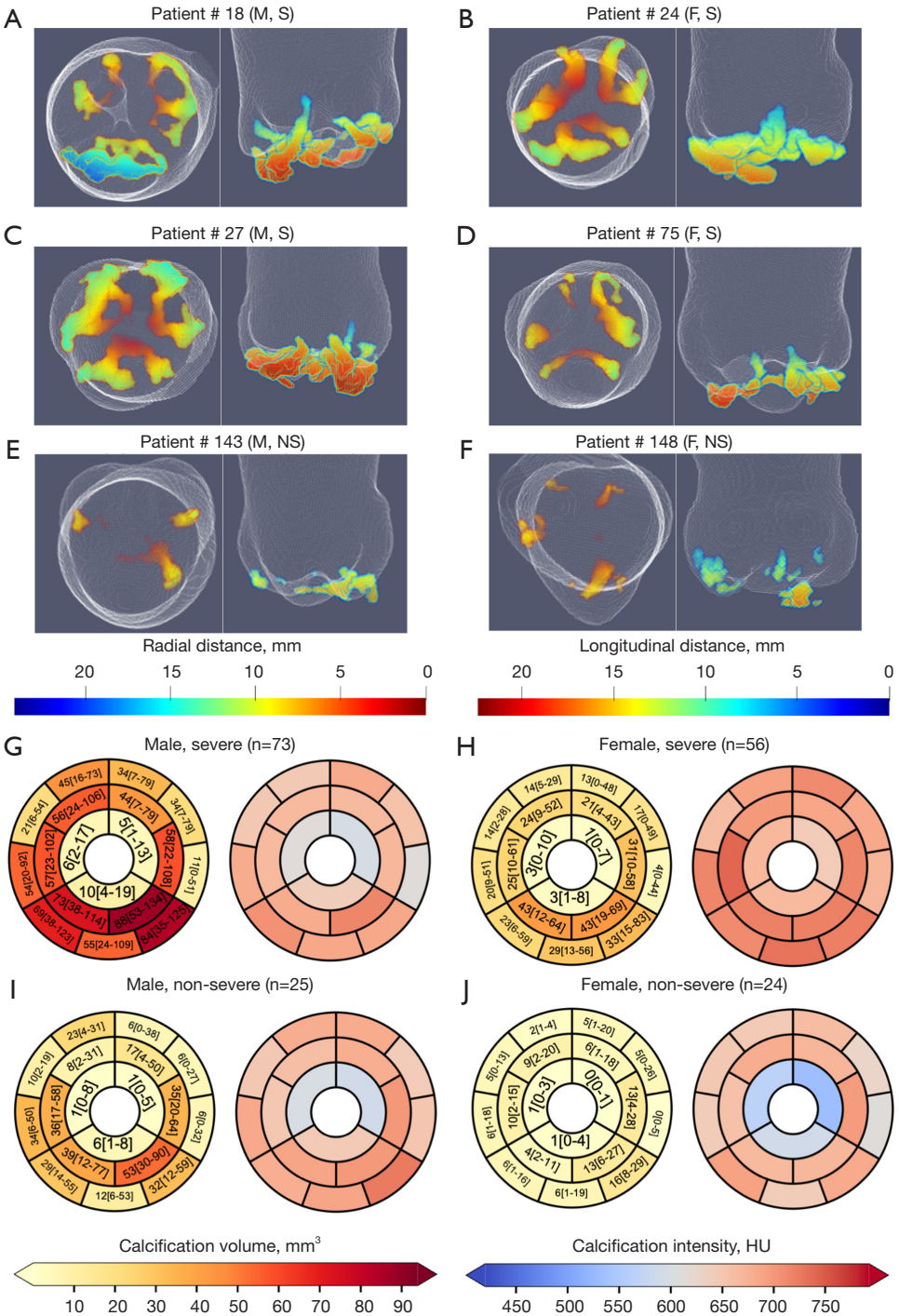

Figure 5 Pattern of calcification in AS (contrast, representative cases). (A-F) Six patients were selected around the median volume score grouped by sex (M-F) and AS severity (NS-S). The left panel shows the detected calcification, color mapped by a normalized radial distance range of (0–25.4 mm). The right panel shows the detected calcification, color mapped by a normalized longitudinal distance range of (0–23.4 mm). Regional volume, annular center, and annular plane proximity (%) were calculated for each leaflet, termed as non-coronary cusp (N), right coronary cusp (R) and left-coronary cusp (L) respectively. (G-J) Bullseye aortic valve plot with 18 region maps described in *Figure 1C* median values for each categorical group (sex and severity) were used to color the volume and HU intensity map. For the volume maps median (IQR) values were annotated inside the borders of each region. AS, aortic stenosis; M, male; F, female; NS, non-severe; S, severe; IQR, interquartile range.

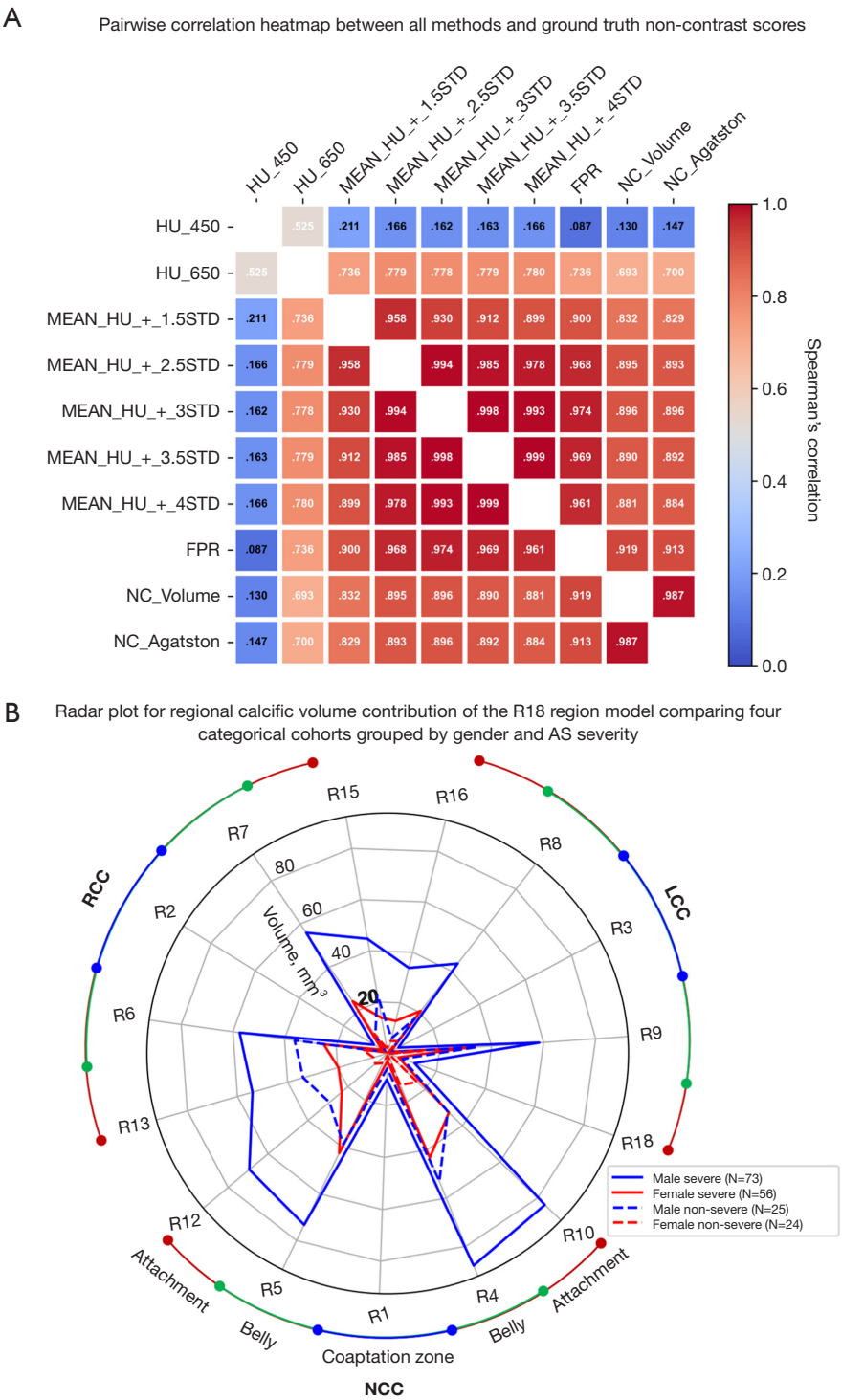

Figure 6 Comparative analysis of calcific detection methods and regional distribution of calcification across the cohort (N=178). (A) Spearman's correlation heatmap between all contrast calcific volume scores and non-contrast volume and Agatston scores. (B) Radar plot with categories grouped by sex and AS severity showing regional median volume spread in each region defined in *Figure 1C*. AS, aortic stenosis.

Table 2 Summary parameter statistics

Parameter	Female		Male	
	Non (n=24)	Severe (n=56)	Non (n=25)	Severe (n=73)
Contrast CT calcific volume (mm^3)	148 [115–209]	473 [374–759]	538 [302–737]	1,133 [780–1,483]
Indexed contrast CT calcific volume (mm^3/cm^2)	39 [26–57]	125 [84–215]	114 [61–143]	215 [172–302]
FPR derived calcific threshold (HU)	462 [423–533]	443 [391–591]	424 [348–491]	375 [307–415]
Non-contrast calcific volume (mm^3)	834 [615–1,094]	2,042 [1,434–2,878]	1,716 [1,374–2,227]	3,281 [2,672–4,363]
Non-contrast Agatston score (AU)	707 [516–867]	1,570 [1,197–2,205]	1,445 [1,145–1,820]	2,645 [2,094–3,460]
Contrast CT calcific volume				
NCC (mm^3)	64 [26–102]	209 [136–353]	246 [123–312]	449 [304–571]
RCC (mm^3)	36 [24–65]	122 [80–253]	114 [85–151]	343 [210–483]
LCC (mm^3)	44 [29–96]	153 [76–222]	167 [113–239]	300 [209–494]
Annular area (cm^2)	4.0 [3.3–4.5]	4.1 [3.5–4.5]	5.2 [4.6–5.6]	5.1 [4.5–5.6]
Annular radius (mm)	11.3 [10.2–12]	11.4 [10.6–12]	12.9 [12.1–13.3]	12.7 [12.0–13.4]
STJ height (mm)	19.7 [18–21]	20.5 [19.1–22.5]	23.6 [21–25.6]	23.4 [21.1–25.5]

All continuous parameters presented as median [interquartile range]. CT, computed tomography; FPR, false positive rate; HU, Hounsfield unit; NCC, non-coronary cusp; RCC, right coronary cusp; LCC, left coronary cusp; STJ, sino-tubular junction.

Table 3 Summary of one-way ANOVA Kruskal-Wallis post-hoc analysis (N=178)

Region	One-way ANOVA (non-parametric) (Dwass-Steel-Critchlow-Fligner pairwise comparisons)					
	F-NS *vs.* F-S	M-NS *vs.* M-S	F-S *vs.* M-S	F-NS *vs.* M-S	F-S *vs.* M-NS	F-NS *vs.* M-NS
R1	0.197	0.316	0.002	<0.001	0.836	0.102
R2	0.242	0.025	0.046	<0.001	0.886	0.757
R3	0.172	0.363	0.054	<0.001	0.976	0.105
R4	0.006	0.036	<0.001	<0.001	0.681	0.003
R5	<0.001	0.126	0.006	<0.001	0.982	<0.001
R6	0.003	0.136	0.006	<0.001	0.887	<0.001
R7	0.01	<0.001	0.003	<0.001	0.121	0.912
R8	0.008	0.173	0.113	<0.001	0.991	0.203
R9	0.096	0.261	0.023	<0.001	0.947	0.113
R10	0.052	0.002	<0.001	<0.001	0.949	0.264
R11	0.002	0.03	0.041	<0.001	0.603	0.356
R12	0.003	0.008	<0.001	<0.001	0.874	<0.001
R13	0.007	0.027	0.005	<0.001	1	0.068
R14	0.057	0.099	0.161	0.001	0.826	0.447
R15	0.002	0.023	0.001	<0.001	0.979	0.026
R16	0.271	0.054	0.107	0.003	0.816	0.855
R17	0.392	0.298	0.969	0.179	0.515	0.994
R18	0.242	0.987	0.997	0.345	0.955	0.688

Results of regional volume post-hoc pairwise comparisons between categories comparing sex and severity effect on regional calcific distribution, P values reported to three significant figures. R, region; F, female; M, male; S, severe; NS, non-severe.

Table 4 Summary of paired sample t-tests Wilcoxon rank

Paired samples t-test (Wilcoxon W)	Wilcoxon test statistic	P value	Mean difference	Standard error difference
NCC				
Coaptation zone—R1				
Belly left—R4	184	<0.001	−52.182	4.33
Belly right—R5	339	<0.001	−42.766	4.77
Belly left—R4				
Attachment left—R10	8,985	0.056	6.946	4.04
Attachment mid—R11	10,466	<0.001	15.868	4.85
Belly right—R5				
Attachment mid—R11	9,659	0.009	9.758	4.68
Attachment right—R12	9,077	0.079	4.172	3.99
RCC				
Coaptation zone—R2				
Belly posterior—R6	734	<0.001	−33.118	3.57
Belly anterior—R7	739	<0.001	−30.991	3.43
Belly posterior—R6				
Attachment posterior—R13	8,640	0.264	2.969	4.58
Attachment mid—R14	12,006	<0.001	16.889	3.84
Belly anterior—R7				
Attachment mid—R14	11,386	<0.001	13.096	3.79
Attachment anterior—R15	9,823	0.007	7.308	3.59
LCC				
Coaptation zone—R3				
Belly anterior—R8	1,400	<0.001	−24.08	3.15
Belly posterior—R9	830	<0.001	−37.433	4.08
Belly anterior—R8				
Attachment anterior—R16	7,829	0.848	0.464	3.87
Attachment mid—R17	8,967	0.082	4.597	4.17
Belly posterior—R9				
Attachment mid—R17	10,931	<0.001	17.933	4.97
Attachment posterior—R18	11,546	<0.001	20.779	4.77

Entire cohort was used in the analysis, pairs of adjacent regions in each leaflet cusp were used to evaluate statistical differences in regional volume across the valve surface. NCC, non-coronary cusp; RCC, right coronary cusp; LCC, left coronary cusp; R, region.

of agreement] where applicable. Finally, interobserver variability was measured using the intraclass correlation coefficient (ICC; two-way random agreement) for a sub cohort of 49 patients. Statistical significance was considered when the P value was less than 0.05. Detailed information regarding derivation and normalization of relevant parameters is outlined in Appendix 1 (section Normalization of the metrics).

Geometrical and structural map of detected calcification

Once the calcified voxels are detected with FPR, we generate density and topographic maps of both radial and longitudinal measurements for the detected calcific regions (*Figure 1B*). We developed an anatomical, 18 region mapping scheme (*Figure 1C*) based on the following standardized measurements: height to sino-tubular-junction, annular area derived radius and angles of the interleaflet triangle (*Figure 1A*). These measurements were used as distance thresholds (18 regions from coaptation zone to attachment) in order to quantify regional calcific volume and average Hounsfield intensity across the cohort (*Figures 5,6B*). Detailed information regarding methodology and theory is presented in Appendix 1, Figure S1 and Table S2.

Results

This study consisted of patients diagnosed with non-severe (49/178; 27.5%) and severe (129/178; 72.5%) AS. The cohort had an average age of 80.5±7.3 years and included males (98/178; 55.1%) and females (80/178; 44.9%). Baseline characteristics are presented in *Table 1*. Interobserver variability was assessed on a random sub-group of 49 patients using ICC (two-way random agreement) showing excellent reproducibility for the contrast CT calcific volume parameter (ICC: 0.95; 95% CI: 0.94–0.96; raters =2).

FPR method assessment

The contrast and non-contrast segmented calcium volumes were compared for the 8 representative patient samples in *Figure 3*. By focusing the field of view on the AV in both contrast and non-contrast images, we can qualitatively compare the patterns of calcification detected between the contrast (FPR method) and non-contrast (standard 130 HU). The detected calcification is identified with a red outline around the region of interest in each subplot (*Figure 3*). In general, we can observe a strong agreement of detected calcification between both images in terms of the shape and location. Additionally, calcification volume using the FPR method showed the best correlation against non-contrast volume and Agatston scores (r=0.919, P<0.001; r=0.913, P<0.001) in contrast-enhanced images (*Figures 4A,6A*). With regards to absolute volume of detected calcification, a large difference is observed. Contrast images consistently produces a lower total volume of detected calcification compared to the non-contrast images. Paired comparisons (*Figures 3,4B*; *Table 2*) showed significantly lower volume scores for the contrast images compared to non-contrast volume scores. This underestimation was observed for all methods evaluated against non-contrast (*Figure 4B*). Visual differences between detected calcific volumes using the proposed method and non-contrast images (130 HU threshold) are presented in (*Figure 3*). Given the systemic bias with non-contrast, we compared FPR with methods based on fixed HU or dynamic HU thresholds using luminal attenuation with Bland-Altman agreement plots (*Figure 4C-4F*), all against the same reference non-contrast volume scores. All evaluated methods showed a proportional bias that increases at higher calcium volumes when compared to non-contrast (*Figure 4C,4D*) with mean luminal attenuation +3SD being the closest method to the FPR (r=0.974; P<0.001) (*Figure 6A*). Moreover, comparative analysis showed the FPR method had the best overall performance in terms of both low and high calcification volumes with a mean bias (1,840.1) and an error at the low and high levels of agreement [–1.96SD: –287.2, +1.96SD: 3,967.5]. Compared to the fixed SD methods, we can clearly observe that at higher SD, bias increases at high level of agreement as the threshold becomes over-conservative in capturing calcific segments. Alternatively, at lower SD, bias increases at the low level of agreement as the determined threshold overestimates calcific segments.

Finally, we can also observe the behavior of the different methods on a representative severe AS patient in *Figure 2B,2C* with high thresholds (+3SD, +4SD) missing small calcific nodules and low thresholds (+1.5SD) merging large calcific regions between the leaflets.

We highlight that luminal attenuation derived methods can over or underestimate calcific deposition, especially in situations of high variance in the blood pool HU intensity distribution or low calcific densities in non-severe cases (16,19). Our FPR method can demonstrably compensate for these limitations, by iterative refinement of HU threshold based on an image specific FPR. This has implications for both a diagnostic use case of contrast-enhanced calcification score and accurate regional assessment of calcific nodules. Precise regional assessment cannot be performed in non-contrast CT due to low contrast and spatial resolution. This is critical as it may provide an incremental improvement over current qualitative criteria of calcification assessment in TAVR planning (6).

Geometry and structure of leaflet calcification in AS

Due to the complex morphology and structure of calcific presentation, the single value scores developed for CAC scoring (11,12) precludes determining the progression of calcific deposition in AS (23,24). The high contrast and spatial resolution in contrast images combined with a precise calcific detection method, provides a unique opportunity to examine the regional presentation of calcific deposition in AS. In that respect, we generated topographic distance maps for both radial and longitudinal distance relative to each patient's AV dimensions (annular radius and STJ height) as presented in *Figure 5A-5E*. We arranged the results of 6 representative patients grouped by sex and AS severity. Furthermore, using the anatomical 18 region mapping scheme described in *Figure 1C*, we evaluated this regional presentation across the entire cohort (*Figure 5G-5J*) both in terms of calcific volume and average Hounsfield intensity in each region. Furthermore, we compared calcific volume contribution between the different groups as well as between the regions for the entire cohort (*Figure 6B*; *Tables 3*,*4*).

In terms of the regional presentation of calcification for each cusp (*Figure 5*), we observed four primary patterns of calcific distribution organized by severity and sex as follows:

(I) Severe: maximal calcific deposition in near the belly region of all leaflets followed by root attachment edges with significantly lower calcification near the coaptation zones (*Figure 5A-5D*,*5G*,*5H*; *Table 4*). In males the amount of calcification is significantly higher across most regions (*Figure 6B*, *Table 3*). While in females (*Figure 5B*,*5D*,*5H*), a lower calcific progression rate presents calcific arcs primarily near free edges of the leaflets that have not yet developed in rings at the fixed edge (*Figure 6B*; *Table 3*).

(II) Non-severe: maximal calcific deposition near sites of root attachment and belly, prominent near the non and left coronary cusps (*Figure 5E*,*5F*,*5I*,*5J*). At this stage calcification primarily presents as disconnected deposits with males presenting significantly higher calcific deposition near leaflet attachment edges between the non and right coronary leaflets than females (*Figure 5F*,*5J*,*6B*; *Table 3*).

Overall, inter-region comparison (*Figure 6B*; *Table 4*) shows a radial spoke pattern of calcific progression that is clustered around the belly region of the leaflets, followed by the root attachment at both sides of the leaflets and significantly decreasing near the coaptation zone. In terms of scale, the non-coronary leaflet experiences the most calcific thickening followed by the right and then left coronary leaflet.

We remark that current *in-vivo* quantitative description of regional calcification is limited (7) and most previous studies relied on excised tissue analysis (23) or biomechanical simulated models (25,26). Our patient specific geometric model was designed to capture the local pattern of calcific deposition. Our results indicate that although calcific progression in each leaflet follows a particular pattern that agrees with previous literature, the rate of calcific progression is clearly asymmetric across the different leaflets. Furthermore, females experience significantly less calcific deposition within those patterns despite experiencing similar degrees of valve obstruction. This observation concurs with recent data (16,27,28), which may add further evidence that calcific thickening alone is not enough to cause significant valve obstruction and subsequent clinical symptoms of AS.

Discussion

AS is generally characterized as a gradual decrease of the valve orifice area leading to LVOT obstruction and later, LV hypertrophy due to an increased afterload. There are two primary pathways for AS development, calcific deposition, and rheumatic heart disease. Globally, calcific AS accounts for the majority of AS pathology particularly in developed countries with prevalence increasing with age. Accurate quantification of calcific burden is therefore critical in the AS diagnostic process, particularly in situations when standard diagnostic measures (e.g., echocardiography) are inconclusive (11).

Current techniques using contrast-enhanced imaging, which are based on luminal attenuation or a fixed HU threshold, have shown promise in terms of ease of use and reproducibility. Despite the benefits, these methods may underestimate calcification in the leaflets, especially if image noise or calcific deposits in the sino-tubular junction (STJ) plane are present. Additionally, these methods may be sensitive to interscan, inter-device and cohort selection, which may explain the wide variation of values used for calcium thresholding (14-19). Thus, we propose an approach that can dynamically adjust the threshold based on local image features. Finally, using high detail contrast imaging, presents a potential to move beyond the bulk volume or Agatston scores (13,16). New markers based on the regional patterns of calcification could be a valuable

add-on to existing CT-TAVR guidance protocols, given that in current CT-TAVR (6) assessment, AS severity is already confirmed and valvular calcification is only described qualitatively to plan interventions. Another motivation for developing new markers for measuring calcific burden is the strong evidence that shape, position, and density distribution of calcification are all closely related to peri-procedural outcomes (6,7,29).

FPR method provides an attenuation stable calcific detection threshold

The key advantage of the FPR method is that by considering a shape overlap measure in guiding the optimization for calcium threshold detection, the method can better adapt to general fluctuations in the intraluminal contrast. Therefore, it can work equally well in both high and low calcific densities. The FPR method (*Figure 2*) relies on the automatic estimation of the FPR of detected contrast material (19) to guide the detection of an optimal threshold of calcific regions. This is based on the idea that the detection of scattered calcific lesions can be guided by the more reliable estimation of the larger AR model with well-defined boundaries. Indeed, the direct evaluation of AS scoring is currently based on non-contrast images (6,11). We showed that the volume scores derived using the proposed method had the strongest correlation with standardized non-contrast calcific scores (*Figure 6A*) and further demonstrated the limitations of fixed and luminal attenuation methods, particularly in either under or overestimation of calcific content at high or low calcific concentrations, respectively (*Figure 4C-4F*). This could be particularly important in improving the reproducibility of calcification assessment using contrast images in large, randomized cohorts, especially in females. Despite exhibiting significantly lower calcific deposition compared to males (*Figure 5*), females still present with symptoms of severe AS (27). In addition, a more precise calcific detection method can have added prognostic use for TAVR planning (6). By determining the regional effect of calcific deposition in periprocedural scenarios (6,7,29) (e.g., paravalvular leakage, left-bundle branch block).

A precise calcium detection method is necessary to accurately evaluate regional calcific distribution and hence understand the more likely pattern of progression. Furthermore, once a calcific threshold is identified, we can proceed to evaluate the HU intensity distribution specific to calcific regions (*Figure 1B*; *Figure 5G-5I*). With higher intensity corresponding to denser calcific concentrations, this may also correspond to earlier vs later calcific deposition (26). From one aspect, diffuse regions may be attributed to late-stage leaflet fibrosis (16). Another aspect of calcification intensity grading is the possibility of predicting leaflet mobility, given that the pattern and rate of calcific progression affects the tissue material properties inducing impairment to physiological function (23-26).

Volume scores for patients with AS in contrast-enhanced images are significantly lower than those using non-contrast images

Previously reported volume scores using contrast images (14,17-19) were considerably lower compared to expected volume scores in AS (21,30). This apparent underestimation, even when using different techniques, was not sufficiently discussed in the literature. Quantifying this bias has important implications for both the diagnostic and prognostic use cases of contrast CT imaging. Indeed, quantifying this relative error in measurement would decrease uncertainty in deriving sex-specific thresholds for AS severity determination. In terms of the comparing contrast and non-contrast calcific estimation, we can observe close qualitative agreement with detected calcification, both in terms of location relative to aortic leaflet surface and pattern of distribution (*Figure 3*). Additionally, we showed significant correlation in volume between both non-contrast and contrast images (*Figure 6A*). Despite these agreements, the total volume scores for contrast images seem to be significantly underestimated compared to those for non-contrast images (*Figures 3*,*4B*; *Table 2*). Potential reasons for this disagreement are as follows (31,32). The non-contrast Agatston protocol uses a lower axial resolution (3 *vs.* 0.625 mm), which may cause an overestimation of large calcific nodules and underestimation of smaller deposits. This is due to the increased slice thickness via the partial volume effect (33). This error would be nonlinear and sensitive to local calcium densities and orientation, which we can observe in our experiments (*Figure 3B*,*3H*; *Figure 4B-4F*). And this also can explain observed underestimation of calcium scores when using the "en-face" reconstructed view (34). Secondly, dense calcific regions with large HU values may produce blooming artifacts (32) which could further compound the volume error with a higher slice thickness. Both factors may imply a more accurate volume measurement using contrast images with lower slice

thickness and contrast differentiation between the tissues.

Varied patterns of calcific distribution can be detected and quantified using contrast CT

In order to better assess calcification in various regions of the cardiovascular system, new quantitative criteria (13) were suggested to go beyond the existing calcification assessment methods (12) which only rely on the quantity of calcification. These markers could be especially important in the context of TAVR planning since different factors can influence the severity of various complications during and post-operation such as the location, quantity, and type of the calcific deposits (6,7,35,36). We have, therefore, developed a geometrical mapping framework that quantifies the topology of the calcification in the AV based on the common anatomical definitions of a tricuspid AV (37,38) and focused on the leaflet region of the valve to provide an *in-vivo* quantitative description of the pattern of calcific progression in AS.

We showed qualitative and quantitative patterns of calcific distribution that seem to closely match those demonstrated in *ex-vivo* studies by Thubrikar *et al.* (23), and those posited in biomechanical simulated models (24-26,38). These experiments chiefly entail the following: calcification advances primarily from the high stress regions of the valve leaflets which form arcs and eventually rings covering the leaflet's surface. Among the four distinctive patterns described previously (24-26), we observed that the primary pattern of calcific arcs forming between the two attachment edges of each leaflet along the belly seems to dominate across sex and severity categories (*Figure 5G-5J*, *Figure 6B*). In severe tricuspid cases, calcific nodules form arcs connecting the root attachment points and eventually form fully connected rings that conform to the free and fixed edge of the leaflets from both sides (*Figure 5*). In contrast, non-severe AS cases have calcification that is less developed and concentrated near the coaptation between the non and left coronary leaflets (*Figure 5*). We also demonstrated that this pattern is presented in both males and females with females experiencing a significantly lower amount across all regions (*Figures 5,6*). Differences in AV size do not sufficiently explain this wide discrepancy (*Table 2*). This finding provides further evidence that biomechanics of functional impairment in females are not dominated by calcific leaflet thickening and it seems that leaflet fibrosis could play a much bigger role in worsening clinical symptoms for females with AS (16,27,28,39). In addition, we further show that asymmetry in cusp sizes and shapes (40) leads to analogous asymmetry in quantity and pattern of calcific distribution across the valve. Regarding regional volume scores, we show a relative increase in non-coronary cusp (NCC) calcification which agrees with previous experiments using similar patient cohorts and image modalities (7) (*Table 2*). The relatively longer length of the NCC (40) along with the direction of calcific progression can explain the discrepancy in volume. This observation could have important implications for post-procedural complications due to the proximity of NCC calcification to the ventricular conduction system (6,7,29). In summary, accurate quantification of the asymmetry in calcific deposits may be important to avoid various procedural complications if related to the positioning and expansion of the implant (7,10,18,41).

This study aims to shed further light on the relationship between calcific leaflet thickening, subsequent valve obstruction and presentation of clinical symptoms (42). A better understanding the biomechanical causes of impaired leaflet mobility may provide an opportunity to decide on optimal intervention times, new staging criteria (43) and personalized patient treatment (44,45).

Limitations

Preliminary findings from this study are based on an observational cohort of patients. Our non-consecutive cohort was chosen to evaluate and verify the proposed methods in a balanced distribution of sex and AS severity which may not reflect in a larger population study. Further investigation is needed in a multi-center setting to better judge the effectiveness of the method in more clinical contexts as well as interscan and inter-device variability. Finally, some of the proposed metrics for calcification assessment should be further analyzed in the context of peri-procedural outcomes in TAVR/TAVI. Future work is needed to develop stronger indices based on these descriptors, which can provide a prognostic impact in relation with implantable device size, type, and expansion behavior.

Conclusions

Calcific AS is the most common valvular disease, with high mortality rate once symptoms are presented. AVR intervention is currently the only treatment option in which AVC deposited in and around the valve is an important factor for procedural risk assessment and predicting complications in TAVR. The presented computational

assessment tool can be used to characterize the complex patterns of calcification at different stages of the disease. We found that calcific progression appears to follow distinctive patterns for each leaflet, with differences emerging in the stage of calcific progression between the leaflets. This difference in rate of progression is also significantly affected by sex which cannot be explained by the difference in valve sizes. In addition, we provide a new method for calcific detection that could potentially overcome the inherent variability of contrast material effect on HU attenuation which could enable additional quantitative criteria for calcific assessment in routinely used contrast CT for TAVR planning. In summary, detailed quantitative description of the complex patterns of leaflet calcification, combined with accurate anatomical assessment of AV morphology, could be critical for simultaneously monitoring the progression of AS, and determining the best treatment options, especially for asymptomatic patients who might eventually need an AV replacement.

Acknowledgments

The authors would like to thank Dr. Tej Sheth (Hamilton Health Sciences and Niagara Health, McMaster University, Hamilton, ON, Canada) and their team for their valuable contributions to this work in terms of access to patient images, demographic information, and baseline characteristics.
Funding: This work was supported by NSERC Discovery Grant (RGPIN-2017-05349). NSERC (https://www.nserc-crsng.gc.ca/index_eng.asp) and the funders had no role in study design, data collection and analysis, decision to publish, or preparation of the manuscript.

Footnote

Conflicts of Interest: All authors have completed the ICMJE uniform disclosure form (available at https://qims.amegroups.com/article/view/10.21037/qims-23-778/coif). The authors have no conflicts of interest to declare.

Ethical Statement: The authors are accountable for all aspects of the work in ensuring that questions related to the accuracy or integrity of any part of the work are appropriately investigated and resolved. The study was conducted in accordance with the Declaration of Helsinki (as revised in 2013). The study was approved by the Hamilton integrated research ethics board (HiREB) and individual consent for this retrospective analysis was waived.

References

1. Clavel MA, Pibarot P. A Decade of Revolutions in Calcific Aortic Stenosis. Cardiol Clin 2020;38:xiii-xiv.
2. Lindman BR, Clavel MA, Mathieu P, Iung B, Lancellotti P, Otto CM, Pibarot P. Calcific aortic stenosis. Nat Rev Dis Primers 2016;2:16006.
3. Généreux P, Stone GW, O'Gara PT, Marquis-Gravel G, Redfors B, Giustino G, Pibarot P, Bax JJ, Bonow RO, Leon MB. Natural History, Diagnostic Approaches, and Therapeutic Strategies for Patients With Asymptomatic Severe Aortic Stenosis. J Am Coll Cardiol 2016;67:2263-88.
4. Siontis GCM, Overtchouk P, Cahill TJ, Modine T, Prendergast B, Praz F, Pilgrim T, Petrinic T, Nikolakopoulou A, Salanti G, Søndergaard L, Verma S, Jüni P, Windecker S. Transcatheter aortic valve implantation vs. surgical aortic valve replacement for treatment of symptomatic severe aortic stenosis: an updated meta-analysis. Eur Heart J 2019;40:3143-53.
5. Pollari F, Hitzl W, Vogt F, Cuomo M, Schwab J, Söhn C, Kalisnik JM, Langhammer C, Bertsch T, Fischlein T, Pfeiffer S. Aortic valve calcification as a risk factor for major complications and reduced survival after transcatheter replacement. J Cardiovasc Comput Tomogr 2020;14:307-13.
6. Blanke P, Weir-McCall JR, Achenbach S, Delgado V, Hausleiter J, Jilaihawi H, Marwan M, Norgaard BL, Piazza N, Schoenhagen P, Leipsic JA. Computed tomography imaging in the context of transcatheter aortic valve implantation (TAVI) / transcatheter aortic valve replacement (TAVR): An expert consensus document of the Society of Cardiovascular Computed Tomography. J Cardiovasc Comput Tomogr 2019;13:1-20.
7. Khalique OK, Hahn RT, Gada H, Nazif TM, Vahl TP, George I, Kalesan B, Forster M, Williams MB, Leon MB, Einstein AJ, Pulerwitz TC, Pearson GD, Kodali SK. Quantity and location of aortic valve complex calcification

predicts severity and location of paravalvular regurgitation and frequency of post-dilation after balloon-expandable transcatheter aortic valve replacement. JACC Cardiovasc Interv 2014;7:885-94.
8. Généreux P, Head SJ, Hahn R, Daneault B, Kodali S, Williams MR, van Mieghem NM, Alu MC, Serruys PW, Kappetein AP, Leon MB. Paravalvular leak after transcatheter aortic valve replacement: the new Achilles' heel? A comprehensive review of the literature. J Am Coll Cardiol 2013;61:1125-36.
9. Pollari F, Dell'Aquila AM, Söhn C, Marianowicz J, Wiehofsky P, Schwab J, Pauschinger M, Hitzl W, Fischlein T, Pfeiffer S. Risk factors for paravalvular leak after transcatheter aortic valve replacement. J Thorac Cardiovasc Surg 2019;157:1406-1415.e3.
10. Mauri V, Deuschl F, Frohn T, Schofer N, Linder M, Kuhn E, Schaefer A, Rudolph V, Madershahian N, Conradi L, Rudolph TK, Schäfer U. Predictors of paravalvular regurgitation and permanent pacemaker implantation after TAVR with a next-generation self-expanding device. Clin Res Cardiol 2018;107:688-97.
11. Pawade T, Sheth T, Guzzetti E, Dweck MR, Clavel MA. Why and How to Measure Aortic Valve Calcification in Patients With Aortic Stenosis. JACC Cardiovasc Imaging 2019;12:1835-48.
12. Agatston AS, Janowitz WR, Hildner FJ, Zusmer NR, Viamonte M Jr, Detrano R. Quantification of coronary artery calcium using ultrafast computed tomography. J Am Coll Cardiol 1990;15:827-32.
13. Blaha MJ, Mortensen MB, Kianoush S, Tota-Maharaj R, Cainzos-Achirica M. Coronary Artery Calcium Scoring: Is It Time for a Change in Methodology? JACC Cardiovasc Imaging 2017;10:923-37.
14. Jilaihawi H, Makkar RR, Kashif M, Okuyama K, Chakravarty T, Shiota T, Friede G, Nakamura M, Doctor N, Rafique A, Shibayama K, Mihara H, Trento A, Cheng W, Friedman J, Berman D, Fontana GP. A revised methodology for aortic-valvar complex calcium quantification for transcatheter aortic valve implantation. Eur Heart J Cardiovasc Imaging 2014;15:1324-32.
15. Alqahtani AM, Boczar KE, Kansal V, Chan K, Dwivedi G, Chow BJ. Quantifying Aortic Valve Calcification using Coronary Computed Tomography Angiography. J Cardiovasc Comput Tomogr 2017;11:99-104.
16. Cartlidge TR, Bing R, Kwiecinski J, Guzzetti E, Pawade TA, Doris MK, Adamson PD, Massera D, Lembo M, Peeters FECM, Couture C, Berman DS, Dey D, Slomka P, Pibarot P, Newby DE, Clavel MA, Dweck MR. Contrast-enhanced computed tomography assessment of aortic stenosis. Heart 2021;107:1905-11.
17. Eberhard M, Mastalerz M, Frauenfelder T, Tanner FC, Maisano F, Nietlispach F, Seifert B, Alkadhi H, Nguyen-Kim TDL. Quantification of aortic valve calcification on contrast-enhanced CT of patients prior to transcatheter aortic valve implantation. EuroIntervention 2017;13:921-7.
18. Bettinger N, Khalique OK, Krepp JM, Hamid NB, Bae DJ, Pulerwitz TC, Liao M, Hahn RT, Vahl TP, Nazif TM, George I, Leon MB, Einstein AJ, Kodali SK. Practical determination of aortic valve calcium volume score on contrast-enhanced computed tomography prior to transcatheter aortic valve replacement and impact on paravalvular regurgitation: Elucidating optimal threshold cutoffs. J Cardiovasc Comput Tomogr 2017;11:302-8.
19. Kim WK, Renker M, Rolf A, Liebetrau C, Van Linden A, Arsalan M, Doss M, Rieck J, Opolski MP, Möllmann H, Walther T, Hamm CW. Accuracy of device landing zone calcium volume measurement with contrast-enhanced multidetector computed tomography. Int J Cardiol 2018;263:171-6.
20. Abdelkhalek M, Daeian M, Chavarria J, Sellers S, Gulsin G, Leipsic J, Sheth T, Keshavarz-Motamed Z. Patterns and Structure of Calcification in Aortic Stenosis: An Approach on Contrast-Enhanced CT Images. JACC Cardiovasc Imaging 2023;16:1224-6.
21. Pawade T, Clavel MA, Tribouilloy C, Dreyfus J, Mathieu T, Tastet L, et al. Computed Tomography Aortic Valve Calcium Scoring in Patients With Aortic Stenosis. Circ Cardiovasc Imaging 2018;11:e007146.
22. Baumgartner H, Hung J, Bermejo J, Chambers JB, Edvardsen T, Goldstein S, Lancellotti P, LeFevre M, Miller F Jr, Otto CM. Recommendations on the Echocardiographic Assessment of Aortic Valve Stenosis: A Focused Update from the European Association of Cardiovascular Imaging and the American Society of Echocardiography. J Am Soc Echocardiogr 2017;30:372-92.
23. Thubrikar MJ, Aouad J, Nolan SP. Patterns of calcific deposits in operatively excised stenotic or purely regurgitant aortic valves and their relation to mechanical stress. Am J Cardiol 1986;58:304-8.
24. Bäck M, Gasser TC, Michel JB, Caligiuri G. Biomechanical factors in the biology of aortic wall and aortic valve diseases. Cardiovasc Res 2013;99:232-41.
25. Arzani A, Mofrad MRK. A strain-based finite element model for calcification progression in aortic valves. J Biomech 2017;65:216-20.
26. Halevi R, Hamdan A, Marom G, Mega M, Raanani E,

Haj-Ali R. Progressive aortic valve calcification: three-dimensional visualization and biomechanical analysis. J Biomech 2015;48:489-97.
27. Myasoedova VA, Di Minno A, Songia P, Massaiu I, Alfieri V, Valerio V, Moschetta D, Andreini D, Alamanni F, Pepi M, Trabattoni D, Poggio P. Sex-specific differences in age-related aortic valve calcium load: A systematic review and meta-analysis. Ageing Res Rev 2020;61:101077.
28. Thaden JJ, Nkomo VT, Suri RM, Maleszewski JJ, Soderberg DJ, Clavel MA, Pislaru SV, Malouf JF, Foley TA, Oh JK, Miller JD, Edwards WD, Enriquez-Sarano M. Sex-related differences in calcific aortic stenosis: correlating clinical and echocardiographic characteristics and computed tomography aortic valve calcium score to excised aortic valve weight. Eur Heart J 2016;37:693-9.
29. Hansson NC, Nørgaard BL, Barbanti M, Nielsen NE, Yang TH, Tamburino C, et al. The impact of calcium volume and distribution in aortic root injury related to balloon-expandable transcatheter aortic valve replacement. J Cardiovasc Comput Tomogr 2015;9:382-92.
30. Angelillis M, Costa G, De Backer O, Mochi V, Christou A, Giannini C, Spontoni P, De Carlo M, Søndergaard L, Miccoli M, Petronio AS. Threshold for calcium volume evaluation in patients with aortic valve stenosis: correlation with Agatston score. J Cardiovasc Med (Hagerstown) 2021;22:496-502.
31. van der Bijl N, de Bruin PW, Geleijns J, Bax JJ, Schuijf JD, de Roos A, Kroft LJ. Assessment of coronary artery calcium by using volumetric 320-row multi-detector computed tomography: comparison of 0.5 mm with 3.0 mm slice reconstructions. Int J Cardiovasc Imaging 2010;26:473-82.
32. Kalisz K, Buethe J, Saboo SS, Abbara S, Halliburton S, Rajiah P. Artifacts at Cardiac CT: Physics and Solutions. Radiographics 2016;36:2064-83.
33. Šprem J, de Vos BD, Lessmann N, van Hamersvelt RW, Greuter MJW, de Jong PA, Leiner T, Viergever MA, Išgum I. Coronary calcium scoring with partial volume correction in anthropomorphic thorax phantom and screening chest CT images. PLoS One 2018;13:e0209318.
34. Guzzetti E, Simard L, Clisson M, Clavel MA. Multiplanar "En Face" Reconstruction of the Aortic Valve: Impact on Aortic Valve Calcium Scoring. JACC Cardiovasc Imaging 2020;13:2678-80.
35. Keshavarz-Motamed Z, Khodaei S, Rikhtegar Nezami F, Amrute JM, Lee SJ, Brown J, Ben-Assa E, Garcia Camarero T, Ruano Calvo J, Sellers S, Blanke P, Leipsic J, de la Torre Hernandez JM, Edelman ER. Mixed Valvular Disease Following Transcatheter Aortic Valve Replacement: Quantification and Systematic Differentiation Using Clinical Measurements and Image-Based Patient-Specific In Silico Modeling. J Am Heart Assoc 2020;9:e015063.
36. Khodaei S, Sadeghi R, Blanke P, Leipsic J, Emadi A, Keshavarz-Motamed Z. Towards a non-invasive computational diagnostic framework for personalized cardiology of transcatheter aortic valve replacement in interactions with complex valvular, ventricular and vascular disease. International Journal of Mechanical Sciences 2021;202–203:106506.
37. Piazza N, de Jaegere P, Schultz C, Becker AE, Serruys PW, Anderson RH. Anatomy of the aortic valvar complex and its implications for transcatheter implantation of the aortic valve. Circ Cardiovasc Interv 2008;1:74-81.
38. Bahadormanesh N, Tomka B, Kadem M, Khodaei S, Keshavarz-Motamed Z. An ultrasound-exclusive non-invasive computational diagnostic framework for personalized cardiology of aortic valve stenosis. Med Image Anal 2023;87:102795.
39. Pantelidis P, Oikonomou E, Lampsas S, Zakynthinos GE, Lysandrou A, Kalogeras K, Katsianos E, Theofilis P, Siasos G, Vavuranakis MA, Antonopoulos AS, Tousoulis D, Vavouranakis M. Lipoprotein(a) and calcific aortic valve disease initiation and progression: a systematic review and meta-analysis. Cardiovasc Res 2023;119:1641-55.
40. Schäfers HJ, Schmied W, Marom G, Aicher D. Cusp height in aortic valves. J Thorac Cardiovasc Surg 2013;146:269-74.
41. Khodaei S, Garber L, Abdelkhalek M, Maftoon N, Emadi A, Keshavarz-Motamed Z. Reducing Long-Term Mortality Post Transcatheter Aortic Valve Replacement Requires Systemic Differentiation of Patient-Specific Coronary Hemodynamics. J Am Heart Assoc 2023;12:e029310.
42. Pawade TA, Newby DE, Dweck MR. Calcification in Aortic Stenosis: The Skeleton Key. J Am Coll Cardiol 2015;66:561-77.
43. Généreux P, Pibarot P, Redfors B, Mack MJ, Makkar RR, Jaber WA, et al. Staging classification of aortic stenosis based on the extent of cardiac damage. Eur Heart J 2017;38:3351-8.
44. Kadem M, Garber L, Abdelkhalek M, Al-Khazraji BK, Keshavarz-Motamed Z. Hemodynamic Modeling, Medical Imaging, and Machine Learning and Their Applications to Cardiovascular Interventions. IEEE Rev Biomed Eng 2023;16:403-23.

45. Mohamed Abdelkhalek, Nikrouz Bahadormanesh, Javier Ganame, Zahra Keshavarz-Motamed, Incremental prognostic value of intensity-weighted regional calcification scoring using contrast CT imaging in TAVR, European Heart Journal - Imaging Methods and Practice, Volume 1, Issue 2, September 2023, qyad027

Cite this article as: Abdelkhalek M, Daeian M, Keshavarz-Motamed Z. Regional assessment of aortic valve calcification using topographic maps in contrast-enhanced CT: *in-vivo* sex and severity-based differences in calcific presentation. Quant Imaging Med Surg 2024;14(1):1-19. doi: 10.21037/qims-23-778

Appendix 1 Supplemental methods

Our developed framework is based on open-source software, Paraview v.5.9.0 (46) for pre-processing and visualization, complimented by in-house Python modules based on Simple ITK v.2.0.2 (47,48) for segmentation and quantification of the regions of interest (*Figure S1*; *Table S2*).

Image pre-processing

Initially, the volumetric CT images, with acquisition parameters detailed in *Table S1*, were loaded into Paraview and the opacity transfer function in the volumetric view was adjusted to highlight soft tissue in the thoracic CT scan, such as vessels and organs (*Figure 1A*). With the aorta clearly visible, the image was then cropped to have a field of view focused on the aortic root, including the interface between the aortic valve and the left ventricular outflow tract (LVOT), a part of the ascending aorta after the sino-tubular junction (STJ) and excluding any other surrounding structures (*Figure 1A*). The field of view is then resampled to have isotropic voxel dimensions of [0.5, 0.5, 0.5 mm].

Valve segmentation

To segment the valve from surrounding tissue, the fast-marching method was employed. This method is closely related to level-set segmentation which is based on solving a partial differential equation (PDE) named the *Eikonal* equation Eq. [1] (49)

$$|\nabla u| = C \quad [1]$$

Where u describes the evolution of a closed surface as a function of time and C represents the cost image which is modeled as the speed of the propagating surface. Fast marching has been shown to segment anatomical regions of complex topology and varied curvature (49). The segmentation process is controlled by seed points where it propagates outward from the local surface normal of the seed points (49). The propagation is controlled by the design of what is known as the speed image or function, which aims to incorporate image features such that high values are present near boundaries and lower values in homogenous regions (49). For our purposes, we first derived a smoothed gradient magnitude image using a gradient magnitude recursive gaussian operation (50) with a smoothing sigma of 0.5. The final speed image was then calculated using a bounded reciprocal operation (50) which produces a new image with values of zero near the boundaries or edges, and values of one in homogeneous regions. The determination of the cost function can be defined as in Eq. [2]

$$C(x) = \frac{1}{1+|\nabla I_g(x)|} \quad [2]$$

Where $C(x)$ denotes the cost and $I_g(x)$ represents the image gradient at some index x. The centroid of the previously annotated field of view (*Figure 2A*) was used as initial seed point, along with the constructed speed image as inputs into a fast-marching procedure (50). The output of which is a time-crossing map, which indicates the time of arrival of the propagated level-set front. This arrival time effectively becomes the number of iterations required segment a particular structure. We therefore set a threshold for this output to a fixed time/level using a binary threshold (50) of 400 iterations, which, we deemed an appropriate value for segmenting the aortic root shape without the calcification in the leaflets. An important implication of how the cost function was designed, is that the segmentation propagates through luminal non-calcified segments that are smoother in the speed image and stop at calcified "sharp" edges in the gradient function.

Finally, to correct for noise and holes in the segmentation and obtain a smoothed surface, we initially used a morphological closing operation (50) with a kernel radius of 2 voxels, and then a smoothing recursive gaussian operation (50) with a kernel radius of 2 voxels. For visualizing the binary volume as a transparent surface, we used the contour filter (51) in Paraview on the final filter output shown in *Figure 1B*. The details of the processing pipeline are shown in a flowchart in *Figure S1* and the detailed parameterization for the various filters is presented in *Table S2*.

https://dx.doi.org/10.21037/qims-23-778

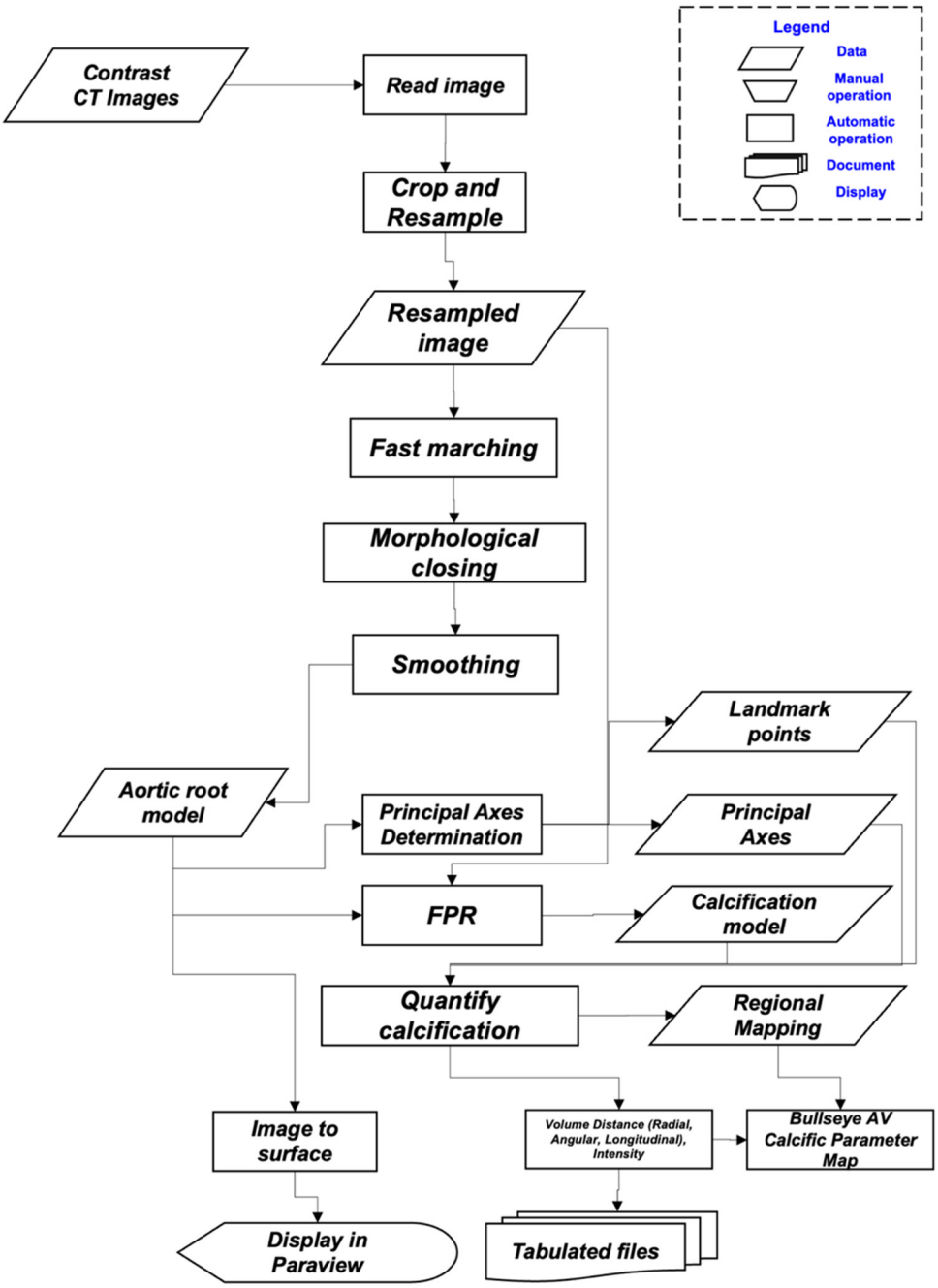

Figure S1 Flowchart diagram of the computational framework developed for assessment of calcification. The flowchart describes a series of operations, either manual or automatic that operate on an initial input set of CT images, to eventually generate tabulated files with relevant clinical indices such as volume scores and display 3D models of detected valve and calcification.

Principal axes determination and landmark points

Once, the smoothed aortic root model is constructed, we proceed to analyze the shape features of the binary segmentation. This is done through shape statistics algorithm (52), which allows us to automatically estimate the orientation axes, the center

https://dx.doi.org/10.21037/qims-23-778

Table S1 CT acquisition information

CT protocol information	CT scanning parameters
Acquisition	Retrospective gated
Slice thickness	0.625 or 3 mm
Tube rotation	0.35 s
Pitch	0.24:1
Tube voltage	120 kV
Tube current	400–500 mA
Reconstruction	ASIR at 30%
Cardiac phase selected	Best diastole (70–75%) cardiac cycle

CT, computed tomography; ASIR, adaptive statistical iterative reconstruction.

of mass and the boundary points of a binary object based on its topology (*Figure 1A*, *Figure S1*, *Table S2*). These principal axes correspond to anatomical short axis view, and two long axis views that are perpendicular to the "En-face" short axis view. These three orientation vectors can be manually corrected by the user, if necessary, to properly orient the desired anatomical views.

We require annotation of four landmark points to complete the analysis. The first landmark point is initialized from the center of mass of the aortic root model and is then corrected such that it falls at the level of the STJ plane and centered at the aortic annulus in the short-axis orientation *Figure 1C*. Next, using the estimated position of the center of the aortic root, the boundary points and the short-axis direction. We proceed to find the maximum elevation points in a directed direction towards the LVOT. These points are then filtered to localize probable location of valve hinge points. The initial location of these three points is corrected manually, such that the points are centered at each cusp and ordered sequentially as NCC, RCC, LCC, respectively *Figure 1D*.

The final STJ point and the orientation axes together uniquely define a new local coordinate system that is relative to the aortic valve leaflets. The basis vectors of this coordinate system A can be computed as an affine transformation Eq. [3], consisting of a rotational Eq. [4] and a translational component Eq. [5]

$$A = \left[\begin{array}{c|c} R & b \\ 0 \cdots 0 & 1 \end{array}\right] \quad [3]$$

such that

$$R = R_Z(\gamma) R_y(\beta) R_x(\alpha) = \begin{bmatrix} \cos\gamma & -\sin\gamma & 0 \\ \sin\gamma & \cos\gamma & 0 \\ 0 & 0 & 1 \end{bmatrix} \begin{bmatrix} \cos\beta & 0 & \sin\beta \\ 0 & 1 & 0 \\ -\sin\beta & 0 & \cos\beta \end{bmatrix} \begin{bmatrix} 1 & 0 & 0 \\ 0 & \cos\alpha & -\sin\alpha \\ 0 & \sin\alpha & \cos\alpha \end{bmatrix} \quad [4]$$

$$\text{and } b = \begin{bmatrix} C_x \\ C_y \\ C_Z \end{bmatrix} \quad [5]$$

The original frame of reference is represented as x, y, z corresponding to anatomic sagittal, coronal, and axial views, respectively (*Figure 1A*, left panel). The rotation angles required to transform the original frame of reference to the local frame are determined from the final "En-face" short axis plane normal (*Figure 1A*, right panel), yielding rotations about the original frame with angles α, β, γ respectively about each axis Eq. [3]. The translation vector b is determined from STJ landmark point defined as C_x, C_y, C_z. The entire affine transformation is later used to realign the image direction, so that the long axis of the valve is now parallel to the unit z and leaflet faces are parallel to the $z = 0$ plane. This is necessary to accurately determine the spatial position of calcific voxels for distance map generation.

https://dx.doi.org/10.21037/qims-23-778

Table S2 Overview of operations/filters used in the platform, input, output and parameters used where applicable

Procedure	Input	Value	Output
Crop and resample	Size	Patient specific	Resampled image [image (HU)]
	Resolution	0.5 mm	
Fast marching	Speed sigma	0.65	Binary mask
	No. of iterations	300	
	Seed point location	Center of aortic root [1]	
Morphological closing	Kernel radius	2	Binary mask
Smoothing	Sigma	0.5	Aortic root model (binary mask)
	Kernel radius	2	
Principal axes determination	Aortic root model	Binary mask [4]	Direction matrix
			Shape boundary
			Geometric center
FPR	Aortic root model	Binary mask [4]	Calcification model (binary mask)
	Resampled image	Image (HU) [1]	
	False positive rate threshold	0.01 = 1%	
Quantify calcification	Calcification model	Binary mask [6]	Regional calcification map (binary mask)
	Principal axes orientation	3×3 direction matrix [5]	Radial distance map (image [mm])
	Landmark points	4 points [5]	Longitudinal distance map (image [mm])
	Volume	Binary mask [6]	Calcification intensity map (image [HU])
Regional mapping	STJ height	Patient specific	Anatomical 18 region volume map
	Annular radius	Derived from patient specific annular area	
	Interleaflet triangle angles	Patient specific	Anatomical 18 region average intensity map
	Calcification model	Binary mask [6]	
	Principal axes orientation	3×3 direction matrix [5]	

Calcium detection [false positive rate (FPR) method]

When viewing the aortic valve (AV) region of interest (ROI) in cases of AS from CT images, we can observe disconnected groups of calcific lesions. These lesions are presented as relatively brighter intensities compared to tissue and lumen. The presence of the contrast agent makes the lower and upper bounds of these intensities practically unknown which is in part due to differences in contrast absorption for each patient (53). Therefore, given that the calcific intensity average will be statistically higher than surrounding objects, a procedure that can grow iteratively from an initial HU estimate is required. The initial estimate of calcific HU threshold is based on average HU of the partial aortic root model. In our proposed implementation we proceed based on the following steps. Using the initial HU estimation, we iteratively increase the HU threshold in steps of 1 HU unit. This is performed exhaustively until a minimum false positive rate criteria is reached (1%).

$$FPR = \frac{C / AR}{C} \quad [6]$$

The (FPR)is defined (54) in set notation as: the ratio between, the no. of pixels in the set difference ($/$) of the aortic root model (AR) segmentation from the calcification model (C) and the total no. of pixels in the calcification model. As the

https://dx.doi.org/10.21037/qims-23-778

threshold is increased, we expect this rate to decrease as the number of luminal pixels mislabeled as calcific decreases. This representation yields a non-linear relationship between the rate and HU threshold of detection which can then be treated as a constrained global minimization problem *Figure 2C*. However, the discrete function representation does not have a global minimum and a specific constraint must be set to avoid overshooting an optimal threshold. We used a minimum of 0.01/1% FPR to stop the iterations and find the optimal threshold. We expect that iterative scheme combined with a global constraint can yield calcific detection thresholds that are robust to variations in intraluminal contrast, calcific density and other image specific factors.

The flowchart of the calcification detection pipeline is shown in *Figure S1* and the parameters used to initialize the shape overlap algorithm is presented in *Table S2*.

Volume and geometric analysis

The final segmented calcium region (*Figure 2A,2B*, red region) is presented as a binary image with values of one in pixels where calcium was detected and values of zero in pixels lacking calcium. We can proceed to determine the volume score based on Eq. [7]

$$\mathrm{Vs} = \left(\sum_{i=0}^{N} M_i \right) \times 0.5^3 \qquad [7]$$

A volume score Vs is calculated by multiplying the total count of ones present on the binary image matrix with the image spacing. Where M_i represents the value of the pixel at index i and N is the total number of pixels. The image spacing due to the previous uniform resampling is 0.5 as mm per direction, giving a total volume score in mm^3.

Since the image volume is now oriented with the long axis of the valve parallel to the Z unit vector, topographic distance maps of the segmented calcium volume can be generated by first converting all pixel coordinates into a physical cartesian coordinate space using the conversion in Eq. [8]

$$\begin{pmatrix} P_1 \\ P_2 \\ P_3 \end{pmatrix} = \begin{pmatrix} O_1 \\ O_2 \\ O_3 \end{pmatrix} + \begin{pmatrix} 1 & 0 & 0 \\ 0 & 1 & 0 \\ 0 & 0 & 1 \end{pmatrix} \times \begin{pmatrix} 0.5 & 0 & 0 \\ 0 & 0.5 & 0 \\ 0 & 0 & 0.5 \end{pmatrix} \times \begin{pmatrix} I_1 \\ I_2 \\ I_3 \end{pmatrix} \qquad [8]$$

$$\begin{pmatrix} P_1' \\ P_2' \\ P_3' \\ 1 \end{pmatrix} = A. \begin{pmatrix} P_1 \\ P_2 \\ P_3 \\ 1 \end{pmatrix} \qquad [9]$$

Where $\vec{P}$ represents the resulting physical space position of an image pixel at some index $\vec{I}$, and $\vec{O}$ is the physical space origin of the first image index. This transformation is automatically handled using the function transform index to physical point (50) and repeated for each pixel index in the image volume. Next, we need to change the basis of each physical coordinate to the local aortic valve system we previously defined in section Calcium detection (shape overlap method). This is accomplished by simple dot product with the transformation matrix that defines the new system Eq. [9].

A conversion from cartesian to cylindrical coordinates can then be applied to $\vec{P}$ for each image pixel, using the transformation in Eq. [10].

$$r = \sqrt{P_1'^2 + P_2'^2}; \quad \theta = \tan^{-1}\left(\frac{P_2'}{P_1'} \right); \quad l = P_3' \qquad [10]$$

These transformations enable the generation of both radial and longitudinal distance maps relative to the aortic sinuses landmark point (*Figure 1B*). Image pixel values are set as r, θ or l for radial, angular and longitudinal maps respectively. These new distance image maps can be then used to introduce the anatomical regional mapping scheme in order to precisely quantify calcific content via the schematic described in *Figure 1C*. The regional map relies on successive binary thresholding

https://dx.doi.org/10.21037/qims-23-778

operations followed by a Boolean intersection (&) operation where in this case the thresholds are determined from the patient specific dimensions of the STJ Height (h), Annular area derived radius (r) and the specific interleaflet triangle angles that demarcate the angular extent of each leaflet (θ_{ncc}, θ_{rcc}, θ_{lcc}). The specific thresholds used as per the proposed 18 region map scheme *Figure 1C* is explicitly described in Eq. [11]. The specific percentage multipliers and patient specific ranges were based on common presentation of a normal tricuspid valve anatomy *Figure 1C* (37) and aim to equalize the area of each region to facilitate comparison with increasing angle divisions as we move towards the attachment from the coaptation zone and fixed radial intervals 0.5r apart.

$$
\mathrm{R}_n = \begin{cases}
\mathrm{R}_1\left(\sum R_i \,\&\, \sum A_i \,\&\, \sum L_i\right) \; s.t:\; 0 \le R_i < 0.25r;\; 0 \le A_i < \theta_{ncc};\; 0.5h \le L_i < h \\
\mathrm{R}_2\left(\sum R_i \,\&\, \sum A_i \,\&\, \sum L_i\right) \; s.t:\; 0 \le R_i < 0.25r;\; \theta_{ncc} \le A_i < \theta_{rcc} + \theta_{ncc};\; 0.5h \le L_i < h \\
\mathrm{R}_3\left(\sum R_i \,\&\, \sum A_i \,\&\, \sum L_i\right) \; s.t:\; 0 \le R_i < 0.25r;\; \theta_{rcc} + \theta_{ncc} \le A_i < \theta_{rcc} + \theta_{ncc} + \theta_{lcc};\; 0.5h \le L_i < h \\
\mathrm{R}_4\left(\sum R_i \,\&\, \sum A_i \,\&\, \sum L_i\right) \; s.t:\; 0.25r \le R_i < 0.75r;\; 0 \le A_i < 0.5\theta_{ncc};\; 0.5h \le L_i < h \\
\mathrm{R}_5\left(\sum R_i \,\&\, \sum A_i \,\&\, \sum L_i\right) \; s.t:\; 0.25r \le R_i < 0.75r;\; 0.5\theta_{ncc} \le A_i < \theta_{ncc};\; 0.5h \le L_i < h \\
\mathrm{R}_6\left(\sum R_i \,\&\, \sum A_i \,\&\, \sum L_i\right) \; s.t:\; 0.25r \le R_i < 0.75r;\; \theta_{ncc} \le A_i < 0.5\theta_{rcc} + \theta_{ncc};\; 0.5h \le L_i < h \\
\mathrm{R}_7\left(\sum R_i \,\&\, \sum A_i \,\&\, \sum L_i\right) \; s.t:\; 0.25r \le R_i < 0.75r;\; 0.5\theta_{rcc} + \theta_{ncc} \le A_i < \theta_{rcc} + \theta_{ncc};\; 0.5h \le L_i < h \\
\mathrm{R}_8\left(\sum R_i \,\&\, \sum A_i \,\&\, \sum L_i\right) \; s.t:\; 0.25r \le R_i < 0.75r;\; \theta_{rcc} + \theta_{ncc} \le A_i < \theta_{rcc} + \theta_{ncc} + 0.5\theta_{lcc};\; 0.5h \le L_i < h \\
\mathrm{R}_9\left(\sum R_i \,\&\, \sum A_i \,\&\, \sum L_i\right) \; s.t:\; 0.25r \le R_i < 0.75r;\; \theta_{rcc} + \theta_{ncc} + 0.5\theta_{lcc} \le A_i < \theta_{rcc} + \theta_{ncc} + \theta_{lcc};\; 0.5h \le L_i < h \\
\mathrm{R}_{10}\left(\sum R_i \,\&\, \sum A_i \,\&\, \sum L_i\right) \; s.t:\; 0.75r \le R_i < 1.25r;\; 0 \le A_i < 0.33\theta_{ncc};\; 0.5h \le L_i < h \\
\mathrm{R}_{11}\left(\sum R_i \,\&\, \sum A_i \,\&\, \sum L_i\right) \; s.t:\; 0.75r \le R_i < 1.25r;\; 0.33\theta_{ncc} \le A_i < 0.66\theta_{ncc};\; 0.5h \le L_i < h \\
\mathrm{R}_{12}\left(\sum R_i \,\&\, \sum A_i \,\&\, \sum L_i\right) \; s.t:\; 0.75r \le R_i < 1.25r;\; 0.66\theta_{ncc} \le A_i < \theta_{ncc};\; 0.5h \le L_i < h \\
\mathrm{R}_{13}\left(\sum R_i \,\&\, \sum A_i \,\&\, \sum L_i\right) \; s.t:\; 0.75r \le R_i < 1.25r;\; \theta_{ncc} \le A_i < 0.33\theta_{rcc} + \theta_{ncc};\; 0.5h \le L_i < h \\
\mathrm{R}_{14}\left(\sum R_i \,\&\, \sum A_i \,\&\, \sum L_i\right) \; s.t:\; 0.75r \le R_i < 1.25r;\; 0.33\theta_{rcc} + \theta_{ncc} \le A_i < 0.66\theta_{rcc} + \theta_{ncc};\; 0.5h \le L_i < h \\
\mathrm{R}_{15}\left(\sum R_i \,\&\, \sum A_i \,\&\, \sum L_i\right) \; s.t:\; 0.75r \le R_i < 1.25r;\; 0.66\theta_{rcc} + \theta_{ncc} \le A_i < \theta_{rcc} + \theta_{ncc};\; 0.5h \le L_i < h \\
\mathrm{R}_{16}\left(\sum R_i \,\&\, \sum A_i \,\&\, \sum L_i\right) \; s.t:\; 0.75r \le R_i < 1.25r;\; \theta_{rcc} + \theta_{ncc} \le A_i < \theta_{rcc} + \theta_{ncc} + 0.33\theta_{lcc};\; 0.5h \le L_i < h \\
\mathrm{R}_{17}\left(\sum R_i \,\&\, \sum A_i \,\&\, \sum L_i\right) \; s.t:\; 0.75r \le R_i < 1.25r;\; \theta_{rcc} + \theta_{ncc} + 0.33\theta_{lcc} \le A_i < \theta_{rcc} + \theta_{ncc} + 0.66\theta_{lcc};\; 0.5h \le L_i < h \\
\mathrm{R}_{18}\left(\sum R_i \,\&\, \sum A_i \,\&\, \sum L_i\right) \; s.t:\; 0.75r \le R_i < 1.25r;\; \theta_{rcc} + \theta_{ncc} + 0.66\theta_{lcc} \le A_i < \theta_{rcc} + \theta_{ncc} + \theta_{lcc};\; 0.5h \le L_i < h
\end{cases}
\qquad [11]
$$

Where R, A and L are distance map images with values for each pixel i defined as the radial, angular and longitudinal distance respectively (Eq. [11]) relative to a point located at the STJ plane and centered in relation to the aortic annulus section Calcium detection (shape overlap method). The procedure finds all pixels that satisfy the cylindrical thresholding criteria in each dimension and then combines all the identified pixels via an intersection/Boolean and operation &. The flowchart of the calcification topographic mapping pipeline is shown in *Figure S1* and *Table S2*, 3D distance image views of the quantification maps on top of the valve surface and the ROI, are shown in *Figure 5A-5F*. The final conformal representation of the measured regional quantities is presented in *Figure 5G-5J*.

Normalization of the metrics

For normalizing the volume scores (Vs_d) of the contrast scores, we defined an approximation of annular radius from the annular area that was measured using CT for all patients as follows (54):

$$
\textit{Indexed Contrast Calcific Volume} = \frac{Vs}{\textit{Annular area}} \qquad [12]
$$

We then estimated the annular radius of a circular aortic annulus using the area as follows:

https://dx.doi.org/10.21037/qims-23-778

$$Annular\ radius = \frac{\sqrt{\frac{Annular\ area}{\pi}}}{2} \quad [13]$$

This normalization procedures are critical to interpret the proposed metrics in the presence of variabilities in valve dimensions, patient size and gender variability (55).

References

46. Ahrens J, Geveci B, Law C. ParaView: An End-User Tool for Large-Data Visualization. In: The Visualization Handbook. 2005.
47. Johnson HJ, McCormick MM. The ITK Software Guide Book 2: Design and Functionality, 4th edition. 552.
48. McCormick M, Liu X, Jomier J, Marion C, Ibanez L. ITK: enabling reproducible research and open science. Front Neuroinform 2014;8:13.
49. Visual Computing for Medicine. Elsevier; 2014 [cited 2021 May 13]. Available online: https://linkinghub.elsevier.com/retrieve/pii/C2011005785X
50. Johnson HJ, McCormick MM, Ibanez L. The ITK Software Guide Book 2: Design and Functionality - Volume 2. Clifton Park, NY, USA: Kitware, Inc.; 2015.
51. Schroeder W, Martin K, Lorensen B. The visualization toolkit: an object-oriented approach to 3D graphics. visualize data in 3D - medical, engineering or scientific; build your own applications with C++, Tcl, Java or Python; includes source code for VTK (supports Unix, Windows and Mac). 4th ed. Clifton Park, NY: Kitware, Inc.; 2006:512.
52. Lehmann G. Label object representation and manipulation with ITK. The Insight Journal 2007 Aug 1 [cited 2022 Mar 15]. Available online: https://www.insight-journal.org/browse/publication/176
53. Pawade T, Sheth T, Guzzetti E, Dweck MR, Clavel MA. Why and How to Measure Aortic Valve Calcification in Patients With Aortic Stenosis. JACC Cardiovasc Imaging 2019;12:1835-48.
54. Tustison NJ, Gee J. Introducing Dice, Jaccard, and Other Label Overlap Measures To ITK. The Insight Journal 2009 Dec 3 [cited 2022 Mar 16]. Available online: https://www.insight-journal.org/browse/publication/707
55. Clavel MA, Messika-Zeitoun D, Pibarot P, Aggarwal SR, Malouf J, Araoz PA, Michelena HI, Cueff C, Larose E, Capoulade R, Vahanian A, Enriquez-Sarano M. The complex nature of discordant severe calcified aortic valve disease grading: new insights from combined Doppler echocardiographic and computed tomographic study. J Am Coll Cardiol 2013;62:2329-38.

https://dx.doi.org/10.21037/qims-23-778